

# Angular Sensing by Highly Reconfigurable Pixel Antennas with Joint Radiating Aperture and Feeding Ports Reconfiguration

Zixiang Han, *Member, IEEE*, Hanning Wang, Shiwen Tang, *Member, IEEE*, and Yujie Zhang, *Member, IEEE*

**Abstract**—Angular sensing capability is realized using highly reconfigurable pixel antenna (HRPA) with joint radiating aperture and feeding ports reconfiguration. Pixel antennas represent a general class of reconfigurable antenna designs in which the radiating surface, regardless of its shape or size, is divided into sub-wavelength elements called pixels. Each pixel is connected to its neighboring elements through radio frequency switches. By controlling pixel connections, the pixel antenna topology can be flexibly adjusted so that the resulting radiation pattern can be reconfigured. However, conventional pixel antennas have only a single, fixed-position feeding port, which is not efficient for angular sensing. Therefore, in this work, we further extend the reconfigurability of pixel antennas by introducing the HRPA, which enables both geometry control of the pixel antenna and switching of its feeding ports. The model of the proposed HRPA, including both circuit and radiation parameters, is derived. A codebook is then defined, consisting of pixel connection states and feeding port positions for each sensing area. Based on this codebook, an efficient optimization approach is developed to minimize the Cramér-Rao lower bound (CRLB) and obtain the optimal HRPA geometries for angular sensing within a given area. Numerical results show that the HRPA reduces the angle estimation error by more than 50% across the full three-dimensional sphere when compared with a conventional uniform planar array of the same size. This demonstrates the effectiveness of the proposed approach and highlights the potential of HRPA for integrated sensing and communication systems.

**Index Terms**—6G, AoA, multi-port, pixel antenna, reconfigurable antenna, sensing.

## I. INTRODUCTION

Integrated sensing and communication (ISAC) is listed as one of the six key usage scenarios in the sixth-generation (6G) mobile network, which is expected to serve many novel applications such as unmanned aerial vehicle (UAV) navigation and vehicle to everything (V2X) regulation [1]. Angle of arrival (AoA) sensing, including azimuth and elevation angle estimation, is one of the major tasks in ISAC systems [2]. Conventional multiple-input multiple-output (MIMO) antennas, such as active antenna unit (AAU) in base stations, employ uniform linear array (ULA) or uniform planar array (UPA) which can be used to determine AoA according to wave

This work was supported in part by NTU Start-up Grant and in part by the Ministry of Education (Singapore) under AcRF TIER1 (RS30/25). (*Corresponding author: Yujie Zhang, e-mail: yujie.zhang@ntu.edu.sg*)

Z. Han and H. Wang are with the Future Research Lab, China Mobile Research Institute, 100053, Beijing, China.

S. Tang is with the Department of Electrical and Computer Engineering, National University of Singapore, Singapore.

Y. Zhang is with School of Electrical and Electronic Engineering, Nanyang Technological University, Singapore.

path difference between the antenna array elements [3]. The wave path difference is dependent on the angular gradient of radiation patterns among antenna elements, which is the largest at the broadside angles for ULA and UPA. However, it degrades significantly at endfire angles. In addition, uniform array is normally not implemented in compact devices, including mobile phones at the user equipment (UE), due to limited size and shape for antenna design. The irregular MIMO antennas at UE receivers further deteriorates the angle estimation performance.

A promising technique to address these issues is utilizing the pixel antennas which are a general reconfigurable antenna design where radiating structure with arbitrary shape and size can be discretized into a subwavelength elements denoted as pixels [4]. Therefore, pixel antennas can fully leverage the given space for antenna in compact devices. The adjacent pixels can be connected or disconnected by using radio frequency (RF) switches such as positive-intrinsic-negative (PIN) diodes. By controlling the pixel connection states, the pixel antenna topology can be flexibly adjusted so that the resulting antenna characteristics such as radiation patterns can be reconfigured. Utilizing this reconfigurability, various of pixel antennas have been designed [5]-[14]. A function of pixel antenna is performing beam-steering where the key advantage is that phase shifters are not needed, avoiding the high insertion loss and reducing the cost of RF front-end when compared to conventional uniform array [5]-[10]. Pixel antennas have also been applied to reconfigurable intelligent surface design [11], [12] and compact antennas decoupling [13]. The cross polarization ratio of radiation pattern can also be by using pixel antennas [14]. In addition, pixel antennas have been utilized to enhance wireless communication. Recently, a novel technique denoted as antenna coding has recently been proposed [15], which refers to using a binary sequence to control the pixel antenna configurations and resulting radiation patterns. Consequently, the channel capacity can be improved through enhancing channel gains or introducing additional modulation in the beamspace [15], [16]. Nevertheless, these designs mainly focus on the enhancement of antenna metrics or wireless communication capabilities, which overlooks their potential in sensing systems. In addition, these pixel antennas have only one feeding port which cannot efficiently perform angular sensing as conventional multiport ULA or UPA.

Another emerging technology is the fluid antenna system (FAS) [17], in which the antenna can dynamically change its position within a small range [18]. The initial FAS utilizes

the fluidity of liquid metal or conductive fluid to achieve antenna movement [19]. However, the tuning speed and accuracy of this approach are limited. Then the concept of FAS has been extended to reconfigurable pixel antennas which mimic antenna movement by altering the antenna radiating aperture [20]. Leveraging its fluidity, the FAS can enhance key performance metrics of MIMO communication systems, including multiplexing gain, diversity gain, spectral efficiency, and energy efficiency [21]-[24]. The FAS can also assist ISAC systems by enhancing beamforming gain towards sensing targets [25], [26]. One of the key characteristics of fluid antenna is port selection where the RF chains can be flexibly switched to the optimal feeding ports to adapt to the channel environment. With this property, fluid antenna naturally fits the sensing scenarios with moving targets. Nevertheless, an effective approach to perform angular sensing using FAS has not yet been explored.

To address the aforementioned issues, we propose the highly reconfigurable pixel antenna (HRPA), which integrates the advantages of pixel antennas with extreme radiating aperture reconfigurability and FASs with highly movable port positions. Compared with conventional angular sensing based on uniform antenna array with fixed antenna elements, which is sensitive to the angle of arrival (AoA) and which are rarely used in compact devices due to size limitations, the proposed multi-port HRPA offers flexible geometry and configurations. By switching feeding ports and adjusting pixel connections, it can generate a set of radiation patterns that enable accurate AoA estimation of sensing targets. The main contributions of this paper are summarized as follows:

*Firstly*, we investigate a novel antenna architecture, the highly reconfigurable pixel antenna (HRPA), which combines both antenna radiating aperture reconfiguration and feeding port selection for angular sensing. The proposed multi-port HRPA can flexibly tune its radiating aperture and feeding ports to generate radiation patterns that adapt to the angles of sensing targets.

*Secondly*, we provide the architecture and the equivalent circuit model of HRPA. The radiation patterns of the multi-port HRPA are derived based on multiport circuit theory as functions of the pixel antenna geometry and port positions.

*Thirdly*, we provide an efficient optimization approach to obtain optimal geometries of HRPA by minimizing Cramér-Rao lower bound (CRLB). A corresponding codebook is then constructed for angular sensing in different sensing areas.

*Finally*, we simulate the angular sensing performance of the HRPA. Numerical results show that by using the HRPA, angle estimation error can be reduced by more than 50% in the three-dimension space compared with a conventional UPA of same size. The performance improvement is the most significant at the endfire angles. These results demonstrate the effectiveness of the proposed HRPA in angular sensing.

*Organization*: Section II introduces the system model of angular sensing using conventional UPA and reconfigurable pixel antennas. Section III presents the HRPA architecture and derives its radiation patterns using the equivalent circuit model. Section IV proposes an optimization approach for obtaining the optimal HRPA geometries. In Section V, the

angular sensing performance of the HRPA is evaluated to demonstrate its effectiveness. Finally, Section VI concludes the work.

*Notation*: Bold lower and upper case letters denote vectors and matrices, respectively. Letters not in bold font represent scalars.  $|a|$ ,  $\Re\{a\}$ ,  $\Im\{a\}$  refers to the modulus, real part and imaginary part of a complex scalar  $a$ , respectively.  $[\mathbf{a}]_i$  and  $\|\mathbf{a}\|$  refer to the  $i$ th entry and  $l_2$ -norm of a vector  $\mathbf{a}$ , respectively.  $\mathbf{A}^T$ ,  $\mathbf{A}^H$ ,  $[\mathbf{A}]_i$  and  $[\mathbf{A}]_{i,j}$  refer to the transpose, conjugate transpose,  $i$ th column and  $(i,j)$ th entry of a matrix  $\mathbf{A}$ , respectively.  $\mathbb{C}$  denotes the complex number sets and  $j = \sqrt{-1}$  denotes an imaginary number.  $\mathcal{CN}(\mu, \sigma^2)$  denotes complex Gaussian distribution with mean  $\mu$  and variance  $\sigma^2$ .  $\mathbf{0}_N$  refers to an  $N$ -dimension zero vector and  $\mathbf{0}_{M \times N}$  refers to an  $M \times N$  zero matrix.  $\mathbf{U}_N$  denotes an  $N \times N$  identity matrix.  $\text{diag}(a_1, \dots, a_N)$  refers to a diagonal matrix with diagonal elements being  $a_1, \dots, a_N$  and  $\text{blkdiag}(\mathbf{A}_1, \dots, \mathbf{A}_N)$  refers to a block diagonal matrix with diagonal matrices being  $\mathbf{A}_1, \dots, \mathbf{A}_N$ .

## II. SYSTEM MODEL

In this section, we firstly introduce the system model for angular sensing and provide the CRLB for angle estimation. Then we describe the angular sensing of HRPA in comparison with the conventional UPA.

### A. Angular Sensing Model

Consider an angular sensing system with the sensing receiver employing  $N$  antennas, we can collect radiation patterns of the  $N$  antennas at angle of  $\Omega$  as  $\mathbf{E}(\Omega) = [\mathbf{e}_1(\Omega), \mathbf{e}_2(\Omega), \dots, \mathbf{e}_N(\Omega)] = [\mathbf{e}_\Theta(\Omega) \mathbf{e}_\Phi(\Omega)] \in \mathbb{C}^{2 \times N}$  where  $\mathbf{e}_\Theta(\Omega) = [e_{\Theta,1}(\Omega), e_{\Theta,2}(\Omega), \dots, e_{\Theta,N}(\Omega)] \in \mathbb{C}^{1 \times N}$  and  $\mathbf{e}_\Phi(\Omega) = [e_{\Phi,1}(\Omega), e_{\Phi,2}(\Omega), \dots, e_{\Phi,N}(\Omega)] \in \mathbb{C}^{1 \times N}$  refer to the steering vector of the  $\Theta$  and  $\Phi$  polarization components respectively.  $\Omega = (\theta, \phi)$  denotes the spatial angle with  $\theta$  and  $\phi$  representing the elevation and azimuth angles in spherical coordinates, respectively. When the angle of the sensing target with respect to the receiver, i.e., angle of arrival (AoA), is  $\Omega$ , we can write the sensing system as

$$\mathbf{y} = \begin{bmatrix} \mathbf{e}_\Theta(\Omega) \\ \mathbf{e}_\Phi(\Omega) \end{bmatrix}^T \begin{bmatrix} s_\Theta \\ s_\Phi \end{bmatrix} + \mathbf{n}, \quad (1)$$

where  $\mathbf{y} \in \mathbb{C}^{N \times 1}$  is the received signal,  $s_\Theta$  and  $s_\Phi$  are source signals for two polarizations and can be regarded as the reflected signal from the sensing object,  $\mathbf{n} \in \mathbb{C}^{N \times 1}$  is the additive Gaussian noise. It should be noted that this model is general for both monostatic and bistatic sensing system.

The angle estimation accuracy at  $\Omega$  can be evaluated by CRLB matrix [27], which can be defined as

$$\mathbf{C}(\Omega) = \frac{\Re\{\mathbf{F}(\Omega)\}^{-1}}{2\text{SNR}} = \begin{bmatrix} c_{\theta\theta} & c_{\theta\phi} \\ c_{\phi\theta} & c_{\phi\phi} \end{bmatrix} \quad (2)$$

where  $c_{\theta\theta}$  and  $c_{\phi\phi}$  refer to the CRLB for estimation errors of  $\theta$  and  $\phi$  respectively,  $c_{\theta\phi}$  and  $c_{\phi\theta}$  refer to the CRLB for the covariance of the estimation errors between  $\theta$  and  $\phi$  with  $c_{\theta\phi} = c_{\phi\theta}$ , SNR is the signal-to-noise ratio, and  $\mathbf{F}(\Omega)$  is the Fisher information matrix (FIM). Using the Slepian-Bang

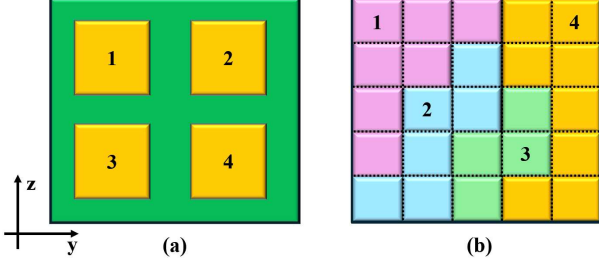


Fig. 1. Illustrative examples of MIMO antennas of (a) conventional UPA and (b) HRPA with  $N = 4$ .

formula, we write the FIM as  $\mathbf{F}(\Omega) = \mathbf{J}^H(\Omega) \mathbf{D}(\Omega) \mathbf{J}(\Omega)$  where the Jacobian matrix  $\mathbf{J}(\Omega) \in \mathbb{C}^{2K \times 2}$  is given by

$$\mathbf{J}(\Omega) = \begin{bmatrix} \frac{\partial \mathbf{e}_\Theta(\Omega)}{\partial \theta} & \frac{\partial \mathbf{e}_\Phi(\Omega)}{\partial \theta} \\ \frac{\partial \mathbf{e}_\Theta(\Omega)}{\partial \phi} & \frac{\partial \mathbf{e}_\Phi(\Omega)}{\partial \phi} \end{bmatrix}^T, \quad (3)$$

and  $\mathbf{D}$  is the projection matrix given by

$$\mathbf{D}(\Omega) = \mathbf{U}_{2K} - \frac{\mathbf{f}(\Omega) \mathbf{f}^H(\Omega)}{\|\mathbf{f}(\Omega)\|^2}, \quad (4)$$

where  $\mathbf{f}(\Omega) = [\mathbf{e}_\Theta(\Omega), \mathbf{e}_\Phi(\Omega)] \in \mathbb{C}^{1 \times 2K}$  collects steering vectors of two polarization components at angle  $\Omega$ . It can be observed from (2) to (4) that entries in the CRLB matrix are related to both polarization components.

### B. Angular Sensing

1) *Angular Sensing by UPA*: Before introducing the HRPA, we firstly describe the angular sensing by a conventional UPA, as illustrated in Fig. 1 (a), where  $N$  identical antenna elements are placed in an  $N_Y \times N_Z$  array with  $N_Y N_Z = N$ . Given the far-field radiation pattern at spatial angle  $\Omega$  of the first antenna element as  $\mathbf{e}_1(\Omega) = [e_{\Theta,1}(\Omega) \ e_{\Phi,1}(\Omega)]^T \in \mathbb{C}^{2 \times 1}$ , we can write the radiation pattern of the  $n$ th antenna element,  $n = 1, 2, \dots, N$ , using the array factor as

$$\mathbf{e}_n(\Omega) = e^{jk((n_y-1)\sin\theta\sin\phi+(n_z-1)\cos\theta)} \mathbf{e}_1(\Omega) \quad (5)$$

where  $k = \frac{2\pi d}{\lambda}$  with  $d$  and  $\lambda$  being the separation distance between the adjacent antenna elements and the wavelength,  $n_y = n \bmod N_Y$  and  $n_z = \left\lceil \frac{n}{N_Y} \right\rceil$  refer to the antenna position in the UPA.

Taking (5) into (2) to (4), the CRLB matrix (2) is given by

$$\mathbf{C}_{\text{UPA}}(\Omega) = \frac{\begin{bmatrix} b_{\text{UPA},\theta\theta} & b_{\text{UPA},\theta\phi} \\ b_{\text{UPA},\phi\theta} & b_{\text{UPA},\phi\phi} \end{bmatrix}}{2k^4 B_Y B_Z \sin^2\theta \cos^2\phi \text{SNR}} \quad (6)$$

where  $b_{\text{UPA},\theta\theta} = B_Y \sin^2\theta \cos^2\phi$ ,  $b_{\text{UPA},\theta\phi} = b_{\text{UPA},\phi\theta} = -B_Y \cos\theta \sin\theta \cos\phi \sin\phi$ , and  $b_{\text{UPA},\phi\phi} = B_Z \sin^2\theta + B_Y \cos^2\theta \sin^2\phi$  with  $B_Y = \frac{N_Y(N_Y^2-1)}{12}$  and  $B_Z = \frac{N_Z(N_Z^2-1)}{12}$ . We can observe from (6) that the angular sensing accuracy of conventional UPA varies greatly in terms of AoA. The minimum CRLB for estimation errors of  $\theta$  and  $\phi$  can be achieved when  $\theta = 90^\circ$  and  $\phi = 0^\circ$  in the broadside direction while CRLBs approach infinity in the endfire directions so that the AoA of sensing targets cannot be estimated when locating on the  $yo_z$  plane.

2) *Angular Sensing by HRPA*: To address the aforementioned issue, in this work, we consider using HRPA to perform angular sensing. Compared with fixed antenna elements and formation as in conventional UPA, HRPA is able to flexibly adjust antenna geometries by selecting feeding ports or changing pixel connections. As illustrated in Fig. 1 (b), a square HRPA with the same aperture as conventional UPA consists of  $N$  different and irregular regions (by solid lines) each of which can be viewed as one antenna element and excited by a single feeding port. The shape and feeding position of these  $N$  elements can be changed (by dashed lines) to various configurations. Therefore, (5) is no longer effective for HRPA.

We write the geometry configuration of HRPA as a variable set  $\mathcal{X}$  so that we have the  $N$  radiation patterns of HRPA as  $\mathbf{E}(\mathcal{X}, \Omega) = [\mathbf{e}_1(\mathcal{X}, \Omega), \dots, \mathbf{e}_N(\mathcal{X}, \Omega)] = [\mathbf{e}_\Theta(\mathcal{X}, \Omega) \ \mathbf{e}_\Phi(\mathcal{X}, \Omega)] \in \mathbb{C}^{2 \times N}$  where  $\mathbf{e}_n(\mathcal{X}, \Omega) = [e_{\Theta,n}(\mathcal{X}, \Omega) \ e_{\Phi,n}(\mathcal{X}, \Omega)]^T \in \mathbb{C}^{2 \times 1}$ ,  $n = 1, 2, \dots, N$  denotes the radiation pattern of the  $n$ th feeding port,  $\mathbf{e}_\Theta(\mathcal{X}, \Omega) = [e_{\Theta,1}(\mathcal{X}, \Omega), e_{\Theta,2}(\mathcal{X}, \Omega), \dots, e_{\Theta,N}(\mathcal{X}, \Omega)] \in \mathbb{C}^{1 \times N}$  and  $\mathbf{e}_\Phi(\mathcal{X}, \Omega) = [e_{\Phi,1}(\mathcal{X}, \Omega), e_{\Phi,2}(\mathcal{X}, \Omega), \dots, e_{\Phi,N}(\mathcal{X}, \Omega)] \in \mathbb{C}^{1 \times N}$  refer to the radiation pattern of the  $\Theta$  and  $\Phi$  polarization components. The CRLB matrix for angle estimation using HRPA is thus given by

$$\mathbf{C}_{\text{RPA}}(\Omega) = \frac{\begin{bmatrix} b_{\text{RPA},\theta\theta} & b_{\text{RPA},\theta\phi} \\ b_{\text{RPA},\phi\theta} & b_{\text{RPA},\phi\phi} \end{bmatrix}}{2B_{\text{RPA}} \text{SNR}} \quad (7)$$

where  $b_{\text{RPA},\theta\theta} = \left\| \frac{\partial \mathbf{f}_{\text{RPA}}(\Omega)}{\partial \theta} \right\|^2$ ,  $b_{\text{RPA},\phi\phi} = \left\| \frac{\partial \mathbf{f}_{\text{RPA}}(\Omega)}{\partial \phi} \right\|^2$ ,  $b_{\text{RPA},\theta\phi} = \Re \left\{ \frac{\partial \mathbf{f}_{\text{RPA}}(\Omega)}{\partial \theta} \frac{\partial \mathbf{f}_{\text{RPA}}^H(\Omega)}{\partial \phi} \right\}$  with  $B_{\text{RPA}} = b_{\text{RPA},\theta\theta} b_{\text{RPA},\phi\phi} - b_{\text{RPA},\theta\phi}^2$  and  $\mathbf{f}_{\text{RPA}}(\Omega) = [\mathbf{e}_\Theta(\mathcal{X}, \Omega), \mathbf{e}_\Phi(\mathcal{X}, \Omega)] \in \mathbb{C}^{1 \times 2K}$ . We can observe from (7) that CRLBs for estimation errors of  $\theta$  and  $\phi$  strongly depend on the angular gradient of the HRPA radiation patterns. In general, the uniform antenna array has better performance than non-uniform antenna array in terms of the sensing area of whole 3D sphere. However for HRPA, we can optimize its geometry configuration for given sensing area to maximize the angular gradient of the radiation patterns for performance enhancement. The radiation patterns and sensing performance of HRPA will be provided in the following sections.

### III. HRPA MODEL

In this section, we firstly describe the architecture of the HRPA. Then we derive the radiation patterns of the HRPA, based on the equivalent circuit model, for angular sensing.

#### A. Architecture of HRPA

The architecture of the HRPA is shown in Fig. 2 (a), which is composed by a pixel layer, a ground layer and a feeding port layer that connects the pixel layer and ground layer. The pixel layer is made of a copper surface mounted on a dielectric substrate where the copper surface is discretized into an array with sub-wavelength elements denoted as pixels. Each pair of adjacent pixels is connected by a loaded port which can be implemented by RF switches. By switching on or off the RF

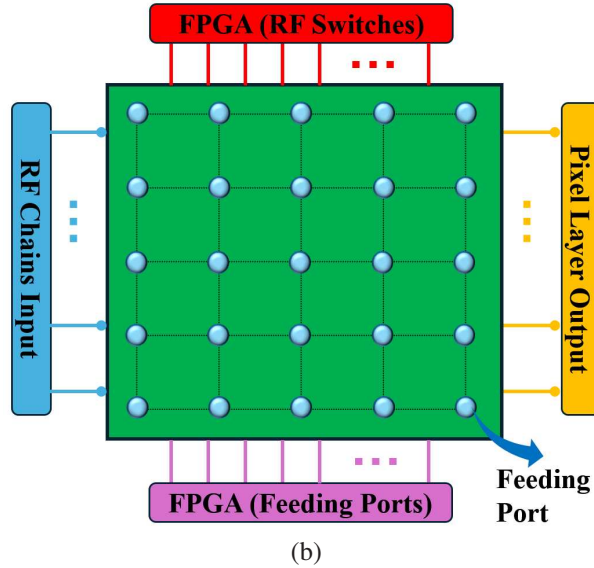
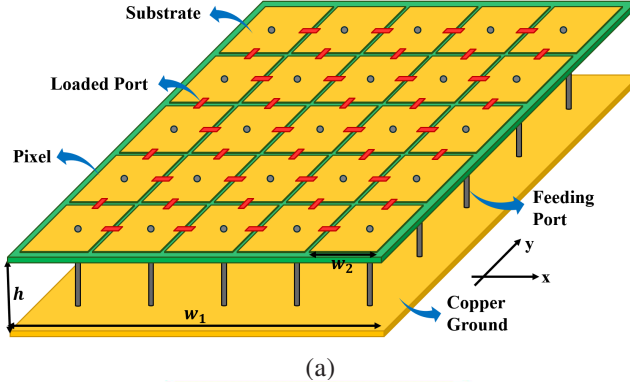


Fig. 2. (a) General architecture and (b) digitally controllable feeding port selection module of HRPA.

switches, the adjacent pixels can be connected or disconnected so that the radiating aperture of the pixel array can be changed. Beneath the pixel layer, a copper plane is placed as the ground so that feeding ports can be set across the ground layer and each of the pixel centers. To control the connection states and partially excite feeding ports, a digitally controllable module, as shown in Fig. 2 (b), based on the Field-Programmable Gate Array (FPGA) is utilized. Particularly, the FPGA set up the connections between the RF chains and the corresponding pixels, determining the activated and muted feeding ports of the HRPA.

The overall diagram for MIMO sensing receiver based on HRPA is shown in Fig. 3 where the number of the activated feeding ports is equal to the number of RF chains. The received sensing signals are processed at the baseband for estimating the AoA. It should be noted that this MIMO antenna diagram is a general design since radiators of arbitrary shape and size can be discretized to form a pixel array and the activation of feeding ports can be performed with the digitally controllable module given arbitrary number of RF chains.

### B. Circuit Model of HRPA

To systematically analyze the architecture of HRPA, we formulate the equivalent circuit model as shown in Fig. 4 in

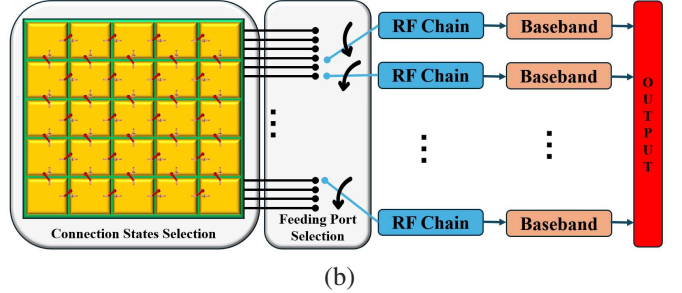


Fig. 3. MIMO sensing receiver diagram using HRPA.

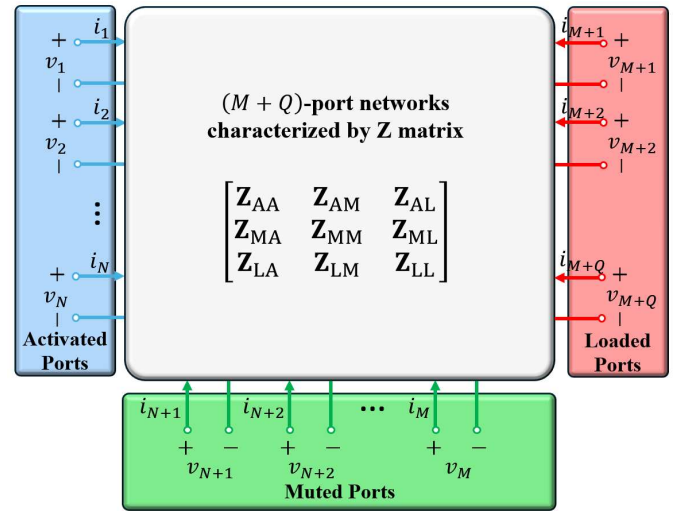


Fig. 4. Equivalent circuit model of  $(M + Q)$ -port network for HRPA with  $N$  activated feeding ports,  $M - N$  muted feeding ports and  $Q$  loaded ports.

which the HRPA is modeled as an  $(M + Q)$ -port network (indexed by  $\{1, 2, \dots, M + Q\}$ ) characterized by a symmetric impedance matrix  $\mathbf{Z} = \mathbf{R} + j\mathbf{X} \in \mathbb{C}^{(M+Q) \times (M+Q)}$  with  $\mathbf{R} = \Re\{\mathbf{Z}\}$  and  $\mathbf{X} = \Im\{\mathbf{Z}\}$  being the resistance and reactance matrix respectively. In addition in HRPA,  $M$  ports are potential feeding ports (indexed by  $\mathcal{M} = \{1, 2, \dots, M\}$ ) and  $Q$  ports are loaded ports (indexed by  $\mathcal{Q} = \{M + 1, M + 2, \dots, M + Q\}$ ).  $N$  RF chains are connected to  $N$  activated feeding ports with the other  $M - N$  ports are muted feeding ports. The open-circuit radiation patterns of the  $(M + Q)$  ports are collected into a matrix  $\mathbf{E}_{oc}(\Omega) = [\mathbf{e}_{oc,1}(\Omega), \mathbf{e}_{oc,2}(\Omega), \dots, \mathbf{e}_{oc,M+Q}(\Omega)] = [\mathbf{e}_{oc,\Theta}(\Omega), \mathbf{e}_{oc,\Phi}(\Omega)] \in \mathbb{C}^{2 \times (M+Q)}$  with  $\mathbf{e}_{oc,\Theta}(\Omega) \in \mathbb{C}^{1 \times (M+Q)}$  and  $\mathbf{e}_{oc,\Phi}(\Omega) \in \mathbb{C}^{1 \times (M+Q)}$  denoting the open-circuit radiation patterns of the  $\Theta$  and  $\Phi$  polarization components respectively. The analysis of the equivalent circuit model is provided in this subsection.

1) *Port Selection*: We start from modeling the feeding port selection of HRPA. Defining the position indices set,  $\mathcal{F} = \{f_1, f_2, \dots, f_N\}$ , which consists of  $N$  different indices of activated feeding ports  $f_n$  with  $1 \leq f_n \leq M$ ,  $n = 1, 2, \dots, N$ , we can write a permutation matrix for feeding port selection given by

$$\mathbf{P}(\mathcal{F}) = [\mathbf{P}_A(\mathcal{F}), \mathbf{P}_M(\mathcal{F}), \mathbf{P}_L] \in \mathbb{C}^{(M+Q) \times (M+Q)} \quad (8)$$

where the  $f_n$ th entry in the  $n$ th column of  $\mathbf{P}_A(\mathcal{F}) \in \mathbb{C}^{(M+Q) \times N}$  is unity with the other entries being zero, which is used to select the  $f_n$ th port as the activated feeding port. In addition,  $\mathbf{P}_L = [\mathbf{0}_{M \times Q}, \mathbf{U}_Q]^T \in \mathbb{C}^{(M+Q) \times Q}$  where the  $q$ th entry,  $q = M+1, M+2, \dots, M+Q$ , in the  $(q-M)$ th column of is unity with the other entries being zero, which denotes the loaded port index and is irrelevant to the feeding port indices as shown in Fig. 4. While each column in  $\mathbf{P}_M(\mathcal{F})$  contains a single unity entry whose position index is included in  $\mathcal{M} \setminus \mathcal{F}$ , indicating the port indices of the muted feeding ports. Using the permutation matrix  $\mathbf{P}(\mathcal{F})$  to select activated feeding ports, we can rearrange the impedance matrix  $\mathbf{Z}$  as

$$\mathbf{P}^T(\mathcal{F}) \mathbf{Z} \mathbf{P}(\mathcal{F}) = \begin{bmatrix} \mathbf{Z}_{AA}(\mathcal{F}) & \mathbf{Z}_{AM}(\mathcal{F}) & \mathbf{Z}_{AL}(\mathcal{F}) \\ \mathbf{Z}_{MA}(\mathcal{F}) & \mathbf{Z}_{MM}(\mathcal{F}) & \mathbf{Z}_{ML}(\mathcal{F}) \\ \mathbf{Z}_{LA}(\mathcal{F}) & \mathbf{Z}_{LM}(\mathcal{F}) & \mathbf{Z}_{LL} \end{bmatrix}, \quad (9)$$

where  $\mathbf{Z}_{AA}(\mathcal{F}) = \mathbf{P}_A^T(\mathcal{F}) \mathbf{Z} \mathbf{P}_A(\mathcal{F}) \in \mathbb{C}^{N \times N}$ ,  $\mathbf{Z}_{MM}(\mathcal{F}) = \mathbf{P}_M^T(\mathcal{F}) \mathbf{Z} \mathbf{P}_M(\mathcal{F}) \in \mathbb{C}^{(M-N) \times (M-N)}$  and  $\mathbf{Z}_{LL} = \mathbf{P}_L^T \mathbf{Z} \mathbf{P}_L \in \mathbb{C}^{Q \times Q}$  are the self impedance sub-matrices of the  $N$  activated feeding ports,  $M-N$  muted feeding ports and  $Q$  loaded ports, respectively.  $\mathbf{Z}_{AM}(\mathcal{F}) = \mathbf{P}_A^T(\mathcal{F}) \mathbf{Z} \mathbf{P}_M(\mathcal{F}) \in \mathbb{C}^{N \times (M-N)}$ ,  $\mathbf{Z}_{AL}(\mathcal{F}) = \mathbf{P}_A^T(\mathcal{F}) \mathbf{Z} \mathbf{P}_L \in \mathbb{C}^{N \times Q}$  and  $\mathbf{Z}_{ML}(\mathcal{F}) = \mathbf{P}_M^T(\mathcal{F}) \mathbf{Z} \mathbf{P}_L \in \mathbb{C}^{(M-N) \times Q}$  are the mutual impedance matrices between all pairs among the activated feeding ports, muted feeding ports and loaded ports respectively with  $\mathbf{Z}_{AM} = \mathbf{Z}_{MA}^T$ ,  $\mathbf{Z}_{AL} = \mathbf{Z}_{LA}^T$  and  $\mathbf{Z}_{ML} = \mathbf{Z}_{LM}^T$ .

Correspondingly, we can also use the permutation matrix to obtain the open-circuit radiation patterns of the activated feeding ports, muted feeding ports and loaded ports as  $\mathbf{E}_A(\mathcal{F}, \Omega) = \mathbf{E}_{oc}(\Omega) \mathbf{P}_A(\mathcal{F})$ ,  $\mathbf{E}_M(\mathcal{F}, \Omega) = \mathbf{E}_{oc}(\Omega) \mathbf{P}_M(\mathcal{F})$  and  $\mathbf{E}_L(\Omega) = \mathbf{E}_{oc}(\Omega) \mathbf{P}_L$ .

2) *Pixel Connections*: Then we model the pixel connection states for the HRPA. A loaded port is placed across each pair of adjacent pixels, which can be implemented by an RF switch. Each RF switch has two states, i.e., switch on and off states, which can be denoted as a binary variable  $g_q \in \{0, 1\}$  for  $q = M+1, M+2, \dots, M+Q$ . The corresponding load impedance can be either open- or short-circuit, written as [15]

$$z_{L,q} = \begin{cases} \infty, & g_q = 1, \text{ i.e. switch off,} \\ 0, & g_q = 0, \text{ i.e. switch on,} \end{cases} \quad (10)$$

where numerically we can use a very large value  $z_{oc}$  to approximate the open-circuit load impedance  $\infty$ . Namely, very large load impedance can make adjacent pixels open-circuited that is equivalent to switching off, while zero load impedance can make adjacent pixel short-circuit that is equivalent to switching on. We collect  $g_q$  into a binary vector  $\mathbf{g} = [g_{M+1}, g_{M+2}, \dots, g_{M+Q}]^T \in \mathbb{R}^{Q \times 1}$  which controls the pixel connection states of HRPA. Accordingly, we can write the load impedance for all  $Q$  loaded ports as a diagonal matrix

$$\begin{aligned} \mathbf{Z}_L^L(\mathbf{g}) &= \text{diag}(z_{L,M+1}, z_{L,M+2}, \dots, z_{L,M+Q}) \\ &= z_{oc} \text{diag}(g_{M+1}, g_{M+2}, \dots, g_{M+Q}). \end{aligned} \quad (11)$$

3) *Overall HRPA Model*: With the open-circuit radiation patterns and impedance matrices, we aim to derive the closed-form expressions for the multi-port HRPA using the multi-port circuit theory. The voltage source excitation at the  $N$

active feeding ports  $v_n$ ,  $n = 1, 2, \dots, N$ , can be grouped into a vector as  $\mathbf{v}_A = [v_1, v_2, \dots, v_N]^T \in \mathbb{C}^{N \times 1}$  while the muted feeding ports are open-circuit which are equivalent to be implemented by zero source voltage  $\mathbf{v}_M = \mathbf{0}_{M-N}$  and infinite inner impedance  $\mathbf{Z}_M^L = \text{diag}(\infty, \infty, \dots, \infty) \in \mathbb{C}^{(M-N) \times (M-N)}$ . The  $Q$  loaded ports are equipped with zero source voltage  $\mathbf{v}_L = \mathbf{0}_Q$ . In addition, we also group currents at the activated feeding ports, muted feeding ports and loaded ports into vectors as  $\mathbf{i}_A = [i_1, i_2, \dots, i_N]^T \in \mathbb{C}^{N \times 1}$ ,  $\mathbf{i}_M = [i_{N+1}, i_{N+2}, \dots, i_M]^T \in \mathbb{C}^{(M-N) \times 1}$  and  $\mathbf{i}_L = [i_{M+1}, i_{M+2}, \dots, i_{M+Q}]^T \in \mathbb{C}^{Q \times 1}$  respectively. Thus we can relate the voltage and current in the  $(M+Q)$ -port network as shown in Fig. 4 (the dependence on  $\mathcal{F}$  and  $\mathbf{g}$  are not shown for brevity) by

$$\begin{aligned} \begin{bmatrix} \mathbf{v}_A \\ \mathbf{v}_M \\ \mathbf{v}_L \end{bmatrix} &= (\mathbf{P}^T \mathbf{Z} \mathbf{P} + \text{blkdiag}(\mathbf{0}, \mathbf{Z}_M^L, \mathbf{Z}_L^L)) \begin{bmatrix} \mathbf{i}_A \\ \mathbf{i}_M \\ \mathbf{i}_L \end{bmatrix} \\ &= \begin{bmatrix} \mathbf{Z}_{AA} & \mathbf{Z}_{AM} & \mathbf{Z}_{AL} \\ \mathbf{Z}_{MA} & \mathbf{Z}_{MM} + \mathbf{Z}_M^L & \mathbf{Z}_{ML} \\ \mathbf{Z}_{LA} & \mathbf{Z}_{LM} & \mathbf{Z}_{LL} + \mathbf{Z}_L^L \end{bmatrix} \begin{bmatrix} \mathbf{i}_A \\ \mathbf{i}_M \\ \mathbf{i}_L \end{bmatrix}. \end{aligned} \quad (12)$$

From (12) we can obtain the relationship between the current at the activated feeding ports and the other ports as

$$\begin{bmatrix} \mathbf{i}_M \\ \mathbf{i}_L \end{bmatrix} = - \begin{bmatrix} \mathbf{Z}_{MM} + \mathbf{Z}_M^L & \mathbf{Z}_{ML} \\ \mathbf{Z}_{LM} & \mathbf{Z}_{LL} + \mathbf{Z}_L^L \end{bmatrix}^{-1} \begin{bmatrix} \mathbf{Z}_{MA} \\ \mathbf{Z}_{LA} \end{bmatrix} \mathbf{i}_A. \quad (13)$$

Since  $\mathbf{Z}_M^L$  is a diagonal matrix with diagonal entries being infinity, (13) can be approximately derived as

$$\begin{aligned} \begin{bmatrix} \mathbf{i}_M \\ \mathbf{i}_L \end{bmatrix} &= \begin{bmatrix} \mathbf{0}_{(M-N) \times (M-N)} & \mathbf{0}_{(M-N) \times Q} \\ \mathbf{0}_{Q \times (M-N)} & -(\mathbf{Z}_{LL} + \mathbf{Z}_L^L)^{-1} \end{bmatrix} \begin{bmatrix} \mathbf{Z}_{MA} \\ \mathbf{Z}_{LA} \end{bmatrix} \mathbf{i}_A \\ &= \begin{bmatrix} \mathbf{0}_{(M-N) \times 1} \\ (\mathbf{Z}_{LL} + \mathbf{Z}_L^L)^{-1} \mathbf{Z}_{LA} \mathbf{i}_A \end{bmatrix}. \end{aligned} \quad (14)$$

Using (14), the impedance matrix among  $N$  activated feeding ports (selected by  $\mathcal{F}$ ) when with pixel connection states  $\mathbf{g}$  can be written as

$$\begin{aligned} \mathbf{Z}_F(\mathcal{F}, \mathbf{g}) &= \mathbf{R}_F(\mathcal{F}, \mathbf{g}) + j\mathbf{X}_F(\mathcal{F}, \mathbf{g}) \\ &= \mathbf{Z}_{AA} - [\mathbf{Z}_{AM}, \mathbf{Z}_{AL}] \cdot \begin{bmatrix} \mathbf{i}_M \\ \mathbf{i}_L \end{bmatrix} \\ &= \mathbf{Z}_{AA} - \mathbf{Z}_{AL} (\mathbf{Z}_{LL} + \mathbf{Z}_L^L)^{-1} \mathbf{Z}_{LA} \end{aligned} \quad (15)$$

where  $\mathbf{R}_F(\mathcal{F}, \mathbf{g}) = \Re\{\mathbf{Z}_F(\mathcal{F}, \mathbf{g})\}$  and  $\mathbf{X}_F(\mathcal{F}, \mathbf{g}) = \Im\{\mathbf{Z}_F(\mathcal{F}, \mathbf{g})\}$  denote the resistance and reactance matrix among  $N$  activated feeding ports. It should be noted that  $\mathbf{Z}_{AA}$ ,  $\mathbf{Z}_{AL}$  and  $\mathbf{Z}_{LA}$  are associated to the activated feeding port indices  $\mathcal{F}$  while  $\mathbf{Z}_{LL}$  is determined by the pixel connection states  $\mathbf{g}$ . Correspondingly, the open-circuit radiation patterns of  $N$  activated feeding ports with pixel connection states  $\mathbf{g}$  can be obtained as

$$\begin{aligned} \mathbf{E}_{oc,F}(\mathcal{F}, \mathbf{g}, \Omega) &= \mathbf{E}_A - [\mathbf{E}_M, \mathbf{E}_L] \cdot \\ &\quad \begin{bmatrix} \mathbf{Z}_{MM} + \mathbf{Z}_M^L & \mathbf{Z}_{ML} \\ \mathbf{Z}_{LM} & \mathbf{Z}_{LL} + \mathbf{Z}_L^L \end{bmatrix}^{-1} \begin{bmatrix} \mathbf{Z}_{MA} \\ \mathbf{Z}_{LA} \end{bmatrix} \\ &= \mathbf{E}_{oc} \left( \mathbf{P}_A - \mathbf{P}_L (\mathbf{Z}_{LL} + \mathbf{Z}_L^L)^{-1} \mathbf{Z}_{LA} \right). \end{aligned} \quad (16)$$

Given the inner impedances of sources at the  $N$  active feeding ports  $\mathbf{Z}_0 = \text{diag}(z_{0,1}, z_{0,2}, \dots, z_{0,N})$  with  $z_{0,n}$ ,  $n = 1, 2, \dots, N$ , denoting the inner impedance of source connected to the  $n$ th activated feeding ports, the radiation patterns of the  $N$  activated feeding ports, including the mutual coupling effect, can be obtained as [13]

$$\mathbf{E}_F(\mathcal{F}, \mathbf{g}, \Omega) = \mathbf{E}_{oc,F}(\mathcal{F}, \mathbf{g}, \Omega) (\mathbf{Z}_0 + \mathbf{Z}_F(\mathcal{F}, \mathbf{g}))^{-1}, \quad (17)$$

where  $\mathbf{E}_F(\mathcal{F}, \mathbf{g}, \Omega) = [\mathbf{e}_{F,\Theta}(\mathcal{F}, \mathbf{g}, \Omega) \ \mathbf{e}_{F,\Phi}(\mathcal{F}, \mathbf{g}, \Omega)] = [\mathbf{e}_{F,1}(\mathcal{F}, \mathbf{g}, \Omega), \dots, \mathbf{e}_{F,N}(\mathcal{F}, \mathbf{g}, \Omega)] \in \mathbb{C}^{2 \times N}$ . In addition, the radiation efficiencies of the  $N$  activated feeding ports can be written as a diagonal matrix  $\Lambda(\mathcal{F}, \mathbf{g}) = \text{diag}(\lambda_1, \lambda_2, \dots, \lambda_N)$  with diagonal entry  $\lambda_n$  referring to the radiation efficiency of the  $n$ th activated feeding port given by

$$\lambda_n(\mathcal{F}, \mathbf{g}) = \frac{\int_{\phi=-\pi}^{\pi} \int_{\theta=0}^{\pi} \mathbf{e}_{F,n}^H \mathbf{e}_{F,n} d\theta d\phi}{\eta \Re \left\{ [\mathbf{v}_A^H]_n \left[ (\mathbf{Z}_0 + \mathbf{Z}_F)^{-1} \mathbf{v}_A \right]_n \right\}} \quad (18)$$

where  $\eta = 120\pi$  is the intrinsic impedance of free space. With (17) and (18), the overall radiation patterns of the proposed HRPA for angular sensing can be obtained as

$$\mathbf{E}(\mathcal{F}, \mathbf{g}, \Omega) = \mathbf{E}_F(\mathcal{F}, \mathbf{g}, \Omega) \Lambda^{\frac{1}{2}}(\mathcal{F}, \mathbf{g}) \quad (19)$$

which includes the effect of both mutual impedances and radiation patterns of  $N$  active feeding ports of HRPA. As a result, by taking (17) into (7) and defining variable set as  $\mathcal{X} = (\mathcal{F}, \mathbf{g})$ , we can obtain CRLB of HRPA, denoted as  $\mathbf{C}_{RPA}(\mathcal{F}, \mathbf{g}, \Omega)$ , to evaluate the angle estimation performance at a given spatial angle  $\Omega$ .

We can use a full electromagnetic solver, CST studio suite [28], to simulate the impedance matrix  $\mathbf{Z}$  and open-circuit radiation patterns  $\mathbf{E}_{oc}(\Omega)$  of all  $(M + Q)$  ports of HRPA. This only needs to be performed once since any impedance matrix and radiation patterns of activated feeding ports can then be found by using (15) and (16) [13].

#### IV. OPTIMIZATION

To obtain the optimal geometries of the proposed HRPA for angular sensing, we wish to select the  $N$  active feeding ports among  $M$  potential feeding ports and optimize the pixel connection states of  $Q$  loaded ports so that CRLB of angular sensing errors in given areas can be minimized. Leveraging the CRLB matrix (2), we can formulate the optimization problem to find the HRPA geometry configuration as

$$\min_{\mathcal{F}, \mathbf{g}} \max \sqrt{\text{Tr}(\mathbf{C}_{RPA}(\mathcal{F}, \mathbf{g}, \Omega))}, \quad (20)$$

$$\text{s.t. } \text{card}(\mathcal{F}) = N, \quad (21)$$

$$\mathbf{g} \in \{0, 1\}^Q. \quad (22)$$

The objective function can evaluate the overall performance of solid angle estimation and aims to simultaneously minimize the maximum CRLB of azimuth and elevation angle estimation for any angle in the sensing area  $\Omega$ . Problem (20) to (22) involves two types of variables, i.e., activated feeding port indices  $\mathcal{F}$  and pixel connection states  $\mathbf{g}$ . There is totally  $\binom{M}{N} \times 2^Q$  possible geometries of HRPA, including  $2^Q$  combinations of pixel connection states and  $\binom{M}{N}$  combinations of activated feeding port indices. Hence, it is impossible to search through all geometries. Besides, the expression of the objective function is also complicated and non-convex. Specifically, altering the activated feeding port indices significantly changes the impedance sub-matrices in (9) and open-circuit radiation patterns in (16) while finding the optimal pixel connection states is a binary optimization problem. For these reasons, it is complicated to solve problem (20) to (22).

To address this issue, we propose an efficient optimization approach, based on alternating optimization method, to iteratively optimize pixel connection states and select activated feeding ports. To start with, the initial guess of the activated feeding port indices and pixel connection states at iteration 0 are denoted as  $\mathcal{F}^{(0)}$  and  $\mathbf{g}^{(0)}$ . At the  $i$ th iteration, we firstly optimize the pixel connection states  $\mathbf{g}^{(i)}$ , with fixed activated feeding port indices  $\mathcal{F}^{(i-1)}$  and the resulting permutation matrix  $\mathbf{P}(\mathcal{F}^{(i-1)})$ , by solving the optimization problem

$$\min_{\mathbf{g}^{(i)}} \max \sqrt{\text{Tr}(\mathbf{C}_{RPA}(\mathcal{F}^{(i-1)}, \mathbf{g}^{(i)}, \Omega))}, \quad (23)$$

$$\text{s.t. } \mathbf{g}^{(i)} \in \{0, 1\}^Q. \quad (24)$$

which is a binary optimization problem. Multiple optimization methods including successive exhaustive Boolean optimization [29], perturbation sensitivity [30] and adjoint method [31] have been proposed. In this work, we use the genetic algorithm (GA) to solve the problem (23)-(24). The optimal pixel connection states are obtained as  $\mathbf{g}^{(i)}$  [6].

We then update the activated feeding port indices  $\mathcal{F}^{(i)}$  by using  $\mathbf{g}^{(i)}$  obtained from problem (23)-(24). This can be formulated as

$$\min_{\mathcal{F}^{(i)}} \max \sqrt{\text{Tr}(\mathbf{C}_{RPA}(\mathcal{F}^{(i)}, \mathbf{g}^{(i)}, \Omega))}, \quad (25)$$

$$\text{s.t. } \text{card}(\mathcal{F}^{(i)}) = N, \quad (26)$$

which is an NP-hard optimization problem. To solve this problem, we use a low-complexity algorithm to sequentially update each entry in  $\mathcal{F}^{(i)}$ . Specifically, we let the optimal index set at the  $(i-1)$ th iteration,  $\mathcal{F}^{(i-1)}$ , to be the initial solution and repeatedly take  $n$  as 1 to  $N$ . When optimizing the  $n$ th activated feeding port index, the other  $N-1$  indices of activated feeding ports are fixed. The  $n$ th activated feeding port index  $f_n$  is selected from the remaining  $M-N+1$  potential feeding ports indices in  $\mathcal{M}$  to minimize the maximum CRLB of azimuth and elevation angle estimation (25), which can be formulated as

$$\min_{f_n} \max \sqrt{\text{Tr}(\mathbf{C}_{RPA}(\mathcal{F}, \mathbf{g}^{(i)}, \Omega))}, \quad (27)$$

$$\text{s.t. } f_n \in (\mathcal{M} \setminus \mathcal{F}^{(i)}) \cup f_n^{(i)}, \quad (28)$$

$$\{\mathcal{F} \setminus f_n\} = \{\mathcal{F}^{(i)} \setminus f_n^{(i)}\}. \quad (29)$$

The objective function value in (27) is descending by sequentially updating each entry in  $\mathcal{F}$  with optimal selection to minimize (27). The algorithm stops when all entries in activated feeding port indices are no longer changed and thus we let  $\mathcal{F}^{(i)} = \mathcal{F}$ . By iteratively optimizing the pixel connection states and activated feeding port positions, the

**Algorithm 1** The alternating optimization method.

---

**Input:**  $\mathcal{X}_{(0),1}^* = (\mathcal{F}_{(0),1}^*, \mathbf{g}_{(0),1}^*)$ ,  $\Omega_{(0)}$ ,  $K_t$ ,  $t = 1, \dots, T$ ;

- 1: **for**  $t = 1: T$
- 2: Equally divide  $\Omega_{(t-1),k}$  into  $K_t$  areas  $\Omega_{(t),k}$ ,  $k = 1, \dots, \prod_{t'=1}^t K_{t'}$ ;
- 3: **for**  $k = 1: \prod_{t'=1}^t K_{t'}$
- 4: **Initialization:**  $\mathcal{F}_{(t),k}^{(0)} = \mathcal{F}_{(t-1),\lfloor (k-1)/\prod_{t'=1}^{t-1} K_{t'} \rfloor + 1}^*$   
 $\mathbf{g}_{(t),k}^{(0)} = \mathbf{g}_{(t-1),\lfloor (k-1)/\prod_{t'=1}^{t-1} K_{t'} \rfloor + 1}^*$ ;
- 5:  $i = 0$ ,
- 6: **repeat**
- 7:  $i = i + 1$ ;
- 8: Find  $\mathbf{g}_{(t),k}^{(i)}$  with  $\mathcal{F}_{(t),k}^{(i-1)}$  by (23) to (24);
- 9: **repeat**
- 10: **for**  $n = 1: N$
- 11: Find  $f_{(t),n}$ ,  $\forall n$  by (27) to (28);
- 12: **end**
- 13: **if**  $\mathcal{F}_{(t),k} = \mathcal{F}_{(t),k}^{(i)}$
- 14: **break**;
- 15: **else**
- 16:  $\mathcal{F}_{(t),k}^{(i)} = \mathcal{F}_{(t),k}$ ;
- 17: **end repeat**
- 18: **until**  $\mathcal{F}_{(t),k}^{(i)} = \mathcal{F}_{(t),k}^{(i-1)}$  and  $\mathbf{g}_{(t),k}^{(i)} = \mathbf{g}_{(t),k}^{(i-1)}$ ;
- 19:  $\mathcal{F}_{(t),k}^* = \mathcal{F}_{(t),k}^{(i)}$  and  $\mathbf{g}_{(t),k}^* = \mathbf{g}_{(t),k}^{(i)}$ ;
- 20: **end**
- 21: **end**

**Output:**  $\mathcal{X}_k^* = (\mathcal{F}_k^*, \mathbf{g}_k^*) = (\mathcal{F}_{(T),k}^*, \mathbf{g}_{(T),k}^*), k = 1, \dots, K$ ;

---

objective function (20) to (22) can converge to a local optimal solution [32].

In the practical implementation, we wish to divide the total radiation space  $\Omega$  into  $K$  sensing areas  $\Omega_k$ ,  $k = 1, 2, \dots, K$  which satisfy  $\bigcup_{k=1}^K \Omega_k = \Omega$  and  $\Omega_k \cap \Omega_l = \emptyset$  for  $k \neq l$ . When the sensing target locates in the area  $\Omega_k$ , the HRPA can use corresponding geometry configuration to excite  $N$  radiation patterns for achieving optimal angular sensing accuracy. To that end, we need to find  $K$  codewords  $\mathcal{X}_k = (\mathcal{F}_k, \mathbf{g}_k)$ ,  $k = 1, 2, \dots, K$ , as the optimal HRPA geometry configurations for  $K$  sensing area  $\Omega_k$ . To efficiently find  $K$  codewords, we propose to use a subdivision method. Specifically at the initial stage, we start from optimizing the HRPA geometry configuration, using the proposed alternating optimization method and initial guess  $\mathcal{X}_{(0)}^* = (\mathcal{F}_{(0)}, \mathbf{g}_{(0)})$ , for the whole radiation space  $\Omega_{(1)} = \bigcup_{k=1}^K \Omega_k$  where the optimal codeword is denoted as  $\mathcal{X}_{(1)}^*$ . Then at the second stage, we can divide the space  $\Omega_{(1)}$  into  $K_2$  areas  $\Omega_{(2),k}$ ,  $k = 1, 2, \dots, K_2$  with the same size satisfying  $\bigcup_{k=1}^{K_2} \Omega_{(2),k} = \Omega$  and  $\Omega_{(2),k} \cap \Omega_{(2),l} = \emptyset$  for  $k \neq l$ , e.g., when  $K_2 = 2$  we have  $\Omega_{(2),1} = \bigcup_{k=1}^{K/2} \Omega_k$  and  $\Omega_{(2),2} = \bigcup_{k=K/2+1}^{K/2} \Omega_k$ . To optimize the codewords for each of the  $K_2$  areas, we use the  $\mathcal{X}_{(1)}^*$  as the initial guess in the alternating optimization method and obtain the optimal codewords as  $\mathcal{X}_{(2),k}^*$ ,  $k = 1, 2, \dots, K_2$ , which can be again used as the initial guess for the next subdivision stage. By repeating this process to divide each of the area  $\Omega_{(t),k}$  into

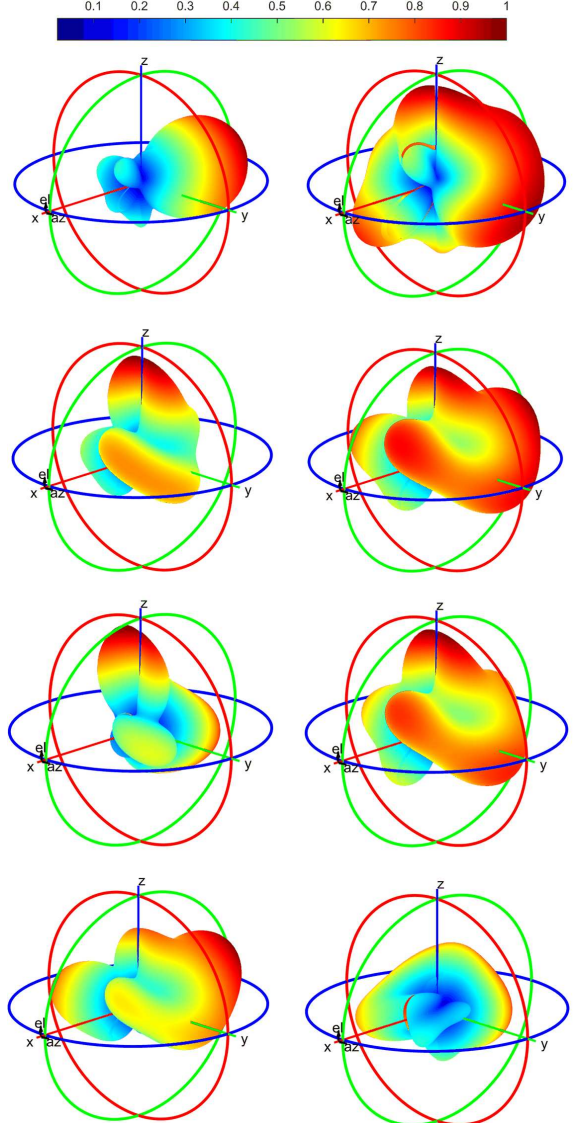


Fig. 5. Radiation patterns of the proposed HRPA with the optimized geometry configurations for optimal sensing at broadside angle  $\theta = 90^\circ$  and  $\phi = 0^\circ$  using  $N = 8$  activated feeding ports.

$K_{t+1}$  areas at the  $t + 1$  stages, we have totally  $K$  areas for  $T$  stages  $\prod_{t=1}^T K_t = K$  ( $K_1$  is set as unity). The  $K$  codewords of the optimal HRPA geometry configurations,  $\mathcal{F}_k^*$  and  $\mathbf{g}_k^*$ ,  $k = 1, 2, \dots, K$ , for  $K$  areas form a codebook that can be used in angular sensing.

Algorithm 1 summarizes the overall algorithm for optimizing the activated feeding port indices and pixel connection states. The performance of the algorithm in finding optimal HRPA geometries will be shown in the next section.

## V. NUMERICAL RESULTS

### A. HRPA Design and Optimization

To demonstrate the performance of the proposed HRPA in angular sensing, we utilize the analysis and optimization approach in Section III and IV to obtain the optimal geometries of HRPA. The HRPA architecture in Fig. 2 is used, which can

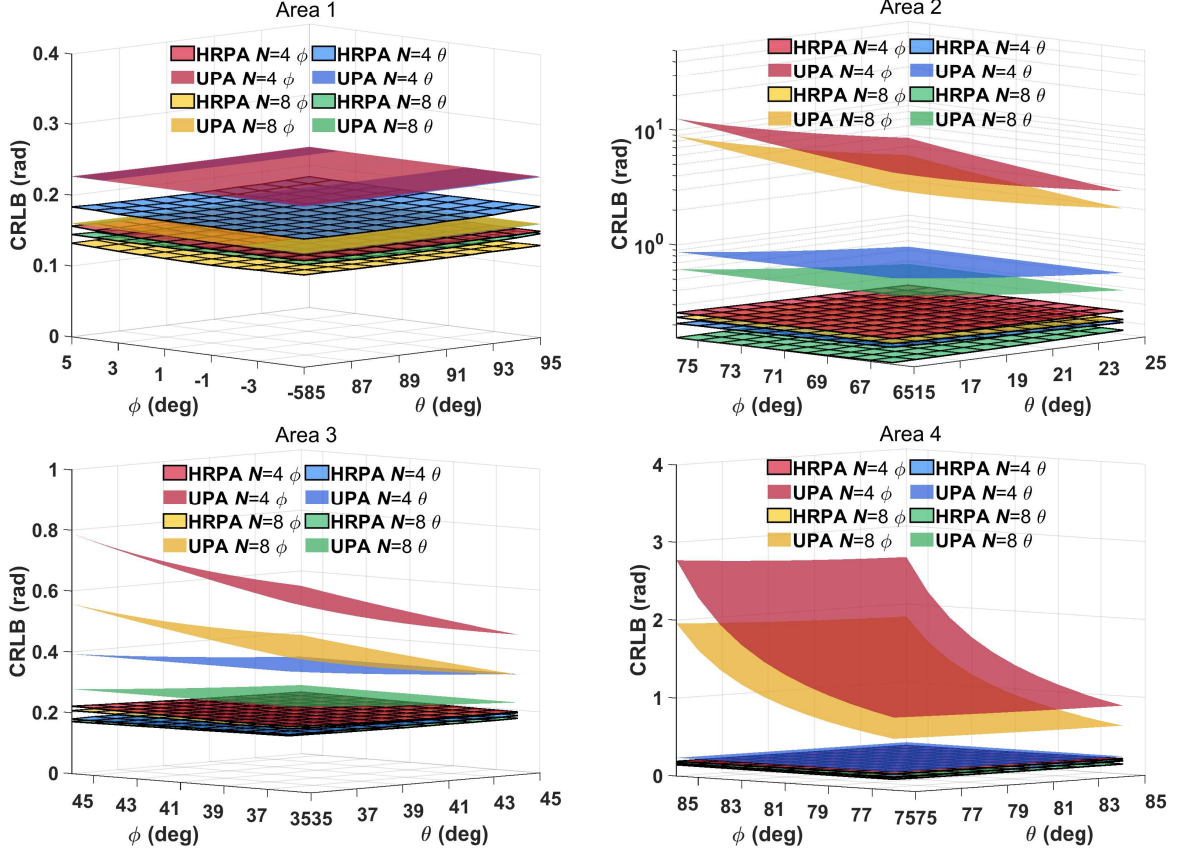


Fig. 6. CRLB of HRPA with  $N = 4$  and  $8$  activated feeding ports in four different sensing areas.

be viewed as discretizing the metal surface of a conventional patch antenna into a  $5 \times 5$  pixel array. The side length of substrate and pixels are  $w_1 = 62.5$  mm and  $w_2 = 12$  mm respectively. The height of the HRPA is  $h = 12.5$  mm. The HRPA has totally 40 loaded ports that can be implemented by RF switches to connect adjacent pixels and 25 potential feeding ports across the pixel array and copper ground. The material of substrate is Rogers 4003C which has thickness of 1.524 mm, permittivity of 3.55 and loss tangent of 0.0027 while the metal is made of copper which has electric conductivity of  $5.8 \times 10^7$  S/m.

We then utilize the Algorithm 1 to obtain the optimal geometries of the HRPA for exciting  $N$  radiation patterns. Specifically, the population size and generation number of GA are set as 500 and 200, respectively. SNR is a constant coefficient in (2) which is set as 0 dB in the following simulation. The resolution of both azimuth and elevation angle are set as  $1^\circ$ . The inner impedance of sources connected to the activated feeding ports, i.e., diagonal entries in  $\mathbf{Z}_0$ , are set as 50 Ohm.

In Fig. 5, we provide the radiation patterns of the proposed HRPA with the optimized geometries for optimal sensing at broadside angle  $\theta = 90^\circ$  and  $\phi = 0^\circ$  using  $N = 8$  activated feeding ports for reference. These are plotted in the full 3D sphere in the far field. We can notice that these radiation patterns are quite different at broadside direction, making the angular gradient large at the broadside angle. Radiation

patterns for the other numbers of activated feeding ports  $N$  and sensing areas follow a similar trend so we omit them.

#### B. Performance of HRPA in Angular Sensing

To demonstrate the proposed HRPA in angular sensing, we utilize the radiation patterns, as illustrated in Fig. 5, to evaluate the performance of HRPA as the MIMO sensing receiver.

1) *CRLB of HRPA in Different Sensing Areas*: We firstly consider the HRPA with  $N = 4$  and  $8$  activated feeding ports. They are benchmarked with a conventional  $2 \times 2$  half-wavelength spaced UPA with single and dual polarization. In addition, we set the size of each sensing area as  $10^\circ \times 10^\circ$ , that is, both azimuth and elevation angle range of each area are  $10^\circ$ . The CRLB results of optimized HRPA geometries, with unit of radians, in angular sensing are shown in Fig. 6 where four sensing areas in different regions of 3D sphere are illustrated, including 1) a broadside angle range  $\theta \in [85^\circ, 95^\circ]$  and  $\phi \in [-5^\circ, 5^\circ]$ , three endfire angle ranges 2)  $\theta \in [15^\circ, 25^\circ]$  and  $\phi \in [65^\circ, 75^\circ]$ , 3)  $\theta \in [35^\circ, 45^\circ]$  and  $\phi \in [35^\circ, 45^\circ]$ , and 4)  $\theta \in [75^\circ, 85^\circ]$  and  $\phi \in [75^\circ, 85^\circ]$ . We can make the following observations.

Firstly, it can be straightforwardly observed that by using the HRPA, the angular sensing accuracy of MIMO receivers for both azimuth and elevation angles can be significantly enhanced in all sensing areas when compared to conventional UPA with fixed antenna geometry. The essence of this performance enhancement is that the geometries of HRPA can be

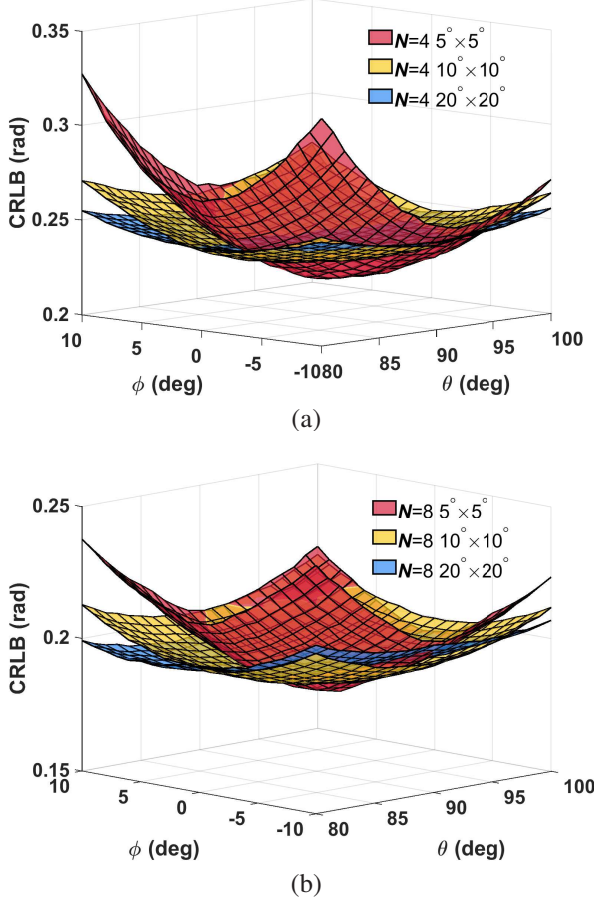


Fig. 7. CRLBs of HRPA with (a)  $N = 4$  and (b)  $N = 8$  activated feeding ports when different size of sensing areas in the optimization are used.

optimized to maximize the pattern angular gradient of HRPA at the given angle, resulting in lower CRLBs. In particular, the angle estimation accuracy can be improved by around 50% in the four areas for both elevation or azimuth angle, demonstrating the effectiveness of the HRPA on enhancing angular sensing of MIMO system.

Secondly, we can observe that the CRLB of HRPA in four sensing areas are generally around 0.2 radians while CRLBs of conventional UPA drastically change in various areas, demonstrating that the HRPA has stable sensing capability for different directions. However, the performance of UPA is more sensitive to the AoA of the sensing targets, i.e., UPA performs best at the broadside angle while its performance rapidly degrades at the endfire angles. For this reason, the performance improvement by the HRPA at the endfire angles is the most significant.

Thirdly, by comparing the results of  $N = 4$  and  $N = 8$ , we can find that the improvement of CRLB for the HRPA from  $N = 4$  to 8 is below 50% in all areas while CRLB of conventional UPA can be halved by using double number of feeding ports. This is because mutual coupling in HRPA becomes stronger when using more activated feeding ports so that radiation efficiencies are reduced, affecting the consequent CRLBs of angle estimation.

2) *CRLB of HRPA with Different Area Size*: Considering that when the target moves to different sensing areas, HRPA needs to switch its geometry configurations to track the target. An HRPA geometry that can cover a larger area while maintaining sensing performance is desired since the switching speed of HRPA geometry configuration can be slower. Therefore, we also investigate the effect of different area size on CRLB of the optimal HRPA geometries. Specifically for cases of  $N = 4$  and 8 activated feeding ports, we select three area size of  $5^\circ \times 5^\circ$ ,  $10^\circ \times 10^\circ$  and  $20^\circ \times 20^\circ$  in the optimization. These three areas are centered at the broadside direction  $\theta = 90^\circ$  and  $\phi = 0^\circ$ . Therefore in the optimization algorithm, the area with the largest size,  $20^\circ \times 20^\circ$ , will be firstly optimized and its optimal geometry configuration is used as the initial point of the optimization afterwards for areas with smaller size  $10^\circ \times 10^\circ$  and  $5^\circ \times 5^\circ$ .

We compare the CRLB results of three geometries, in terms of the overall solid angle estimation (equals to the objective function value in (20)), in the same angle range of  $\theta \in [80^\circ, 90^\circ]$  and  $\phi \in [-10^\circ, 10^\circ]$  as shown in Fig. 7. Two observations can be made.

Firstly, it can be observed that from  $20^\circ \times 20^\circ$  case to  $5^\circ \times 5^\circ$  case, CRLBs of the HRPA are improved within the optimized sensing area, showing that the angular sensing accuracy can be improved when a smaller area size is used in the optimization. However, the number of codewords  $K$  will be larger when with smaller area size so that more HRPA geometry configurations need to be optimized and switching the HRPA geometry is more frequent.

Secondly, we can observe that the CRLB performance of the HRPA degrades when outside the sensing area in the optimization, indicating that the performance enhancement by HRPA within the sensing area is achieved at the expense of the performance degradation in the other areas. A  $10^\circ$  range of azimuth and elevation angles performs good tradeoff between the area size and sensing performance.

3) *CRLB Tradeoff of HRPA*: To further investigate the relationship between the number of activated feeding ports  $N$  and CRLB of the optimal HRPA geometries, we provide CRLB of the overall solid angle estimation, as shown in Fig. 8, when different number of activated feeding ports  $N$  are used. We can make the following observations.

Firstly, we can observe that when  $N < 8$ , CRLBs of the HRPA at different angles decreases as the number of activated feeding ports  $N$  increases. This is because using more activated feeding ports enables a denser spatial sampling through more radiation patterns and thus the pattern angular gradient can be enhanced to reduce CRLB.

Secondly, we can observe that CRLBs approach convergence when  $N \geq 8$ . The reason is that the efficiencies of partial activated feeding ports are very low so that the radiation patterns of these ports make minor contributions to the angular sensing. Therefore, for the designed HRPA with side length of half wavelength,  $N = 8$  activated feeding ports can perform a good tradeoff between the angular sensing accuracy and implementation complexity.

Thirdly, it can be observed that CRLBs of various angle directions are generally close for all number of activated

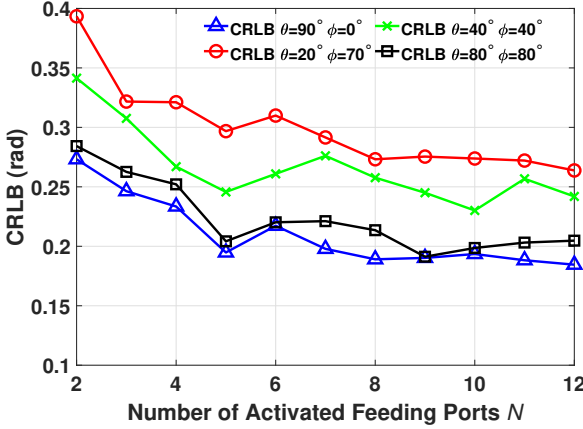


Fig. 8. CRLBs of the HRPA when different number of activated feeding ports are used.

feeding ports, demonstrating again that the proposed HRPA has stable sensing capability for arbitrary angle directions.

To conclude, by using the HRPA to perform angular sensing, the angle estimation accuracy of MIMO receivers can be enhanced. The key advantage of the proposed HRPA approach is that the optimal geometry configurations can be adjusted for targets in various sensing areas to enhance angle estimation performance. The analysis above can provide a guidance for HRPA design and optimization in angular sensing.

## VI. CONCLUSIONS

In this paper, we propose a novel HRPA architecture and investigate its functionality in angular sensing. The proposed multi-port HRPA is extended from the conventional pixel antenna by combining advantages of pixel antennas with extreme radiating aperture reconfigurability and FASs with highly movable port positions. As a result, the geometries of the HRPA can be flexibly changed to adjust the radiation patterns for sensing the angles of targets.

Specifically in this work, the architecture and the equivalent circuit model of HRPA are provided. The radiation patterns of the multi-port HRPA are then derived as a function of pixel connections and port selections. We also develop an efficient alternating optimization approach to obtain the optimal geometries of the HRPA by minimizing CRLB. The resulting geometry configurations form a codebook for angular sensing in different sensing areas. Simulation results show that the proposed HRPA outperforms conventional UPA with same size over the full 3D sphere in angular sensing where the angle estimation accuracy can be improved by more than 50%. The performance improvement at the endfire angles is the most significant. These results demonstrate the effectiveness of the proposed approach and show the promise of HRPA in the sixth generation (6G) ISAC system.

Based on the proposed model in this paper, the artificial intelligence (AI) technique can be further utilized to enhance the HRPA optimization and function in future work. AI is able to perform real-time control of the pixel connections and port selection of HRPA instead of using a codebook

optimized in an offline process. In addition, AI can learn the movement of targets and accurately predict their future directions, thereby reducing the reconfiguration latency in target tracking to support high-mobility scenarios. For these reasons, AI is a powerful tool for real-time sensing and tracking and this direction is left as our first future work.

Another direction for future work is to fabricate a prototype of the HRPA incorporating both variable loads and port selection. The models of practical RF switches and feeding ports can be considered in the optimization and design process. Experimental validation can then be carried out to evaluate the angular sensing accuracy in real-world environments. Overall, the general approach proposed in this work provides a versatile framework for developing compact HRPA designs across various application scenarios, including mobile devices and Internet of Things (IoT) systems.

## REFERENCES

- [1] Z. Zhang, Y. Xiao, Z. Ma, M. Xiao, Z. Ding, X. Lei, G. K. Karagiannidis, and P. Fan, "6G wireless networks: Vision, requirements, architecture, and key technologies," *IEEE Veh. Technol. Mag.*, vol. 14, no. 3, pp. 28–41, 2019.
- [2] W. Xu, C. Zhao, and F. Gao, "Angle domain channel-based camera pose correction for vision-aided ISAC systems," *IEEE Wirel. Commun. Lett.*, vol. 13, no. 8, pp. 2080–2084, 2024.
- [3] Z. Han, H. Ding, X. Zhang, Y. Wang, M. Lou, J. Jin, Q. Wang, and G. Liu, "Multistatic integrated sensing and communication system in cellular networks," in *2023 IEEE Globecom Workshops (GC Wkshps)*, 2023, pp. 123–128.
- [4] B. Cetiner, H. Jafarkhani, J.-Y. Qian, H. J. Yoo, A. Grau, and F. De Flaviis, "Multifunctional reconfigurable MEMS integrated antennas for adaptive MIMO systems," *IEEE Commun. Mag.*, vol. 42, no. 12, pp. 62–70, 2004.
- [5] S. Tang, Y. Zhang, Z. Han, C.-Y. Chiu, and R. Murch, "A pattern-reconfigurable antenna for single-RF 5G millimeter-wave communications," *IEEE Antennas Wirel. Propag. Lett.*, vol. 20, no. 12, pp. 2344–2348, 2021.
- [6] Y. Zhang, Z. Han, S. Tang, S. Shen, C.-Y. Chiu, and R. Murch, "A highly pattern-reconfigurable planar antenna with 360 single- and multi-beam steering," *IEEE Trans. Antennas Propag.*, vol. 70, no. 8, pp. 6490–6504, 2022.
- [7] S. Tang, Y. Zhang, J. Rao, Z. Han, C.-Y. Chiu, and R. Murch, "Beamforming network design utilizing node microstrip architectures for dual-polarized endfire millimeter-wave antenna arrays," *IEEE Trans. Antennas Propag.*, vol. 71, no. 6, pp. 4862–4873, 2023.
- [8] Y. Zhang, S. Tang, Z. Han, J. Rao, S. Shen, M. Li, C.-Y. Chiu, and R. Murch, "A low-profile microstrip vertically polarized endfire antenna with 360 beam-scanning and high beam-shaping capability," *IEEE Trans. Antennas Propag.*, vol. 70, no. 9, pp. 7691–7702, 2022.
- [9] L. Jing, M. Li, and R. Murch, "Compact pattern reconfigurable pixel antenna with diagonal pixel connections," *IEEE Trans. Antennas Propag.*, vol. 70, no. 10, pp. 8951–8961, 2022.
- [10] Y. Zhang, S. Tang, J. Rao, C.-Y. Chiu, X. Chen, and R. Murch, "A dual-port dual-beam pattern-reconfigurable antenna with independent 2-d beam-scanning," *IEEE Transactions on Antennas and Propagation*, vol. 72, no. 10, pp. 7628–7643, 2024.
- [11] J. Rao, Y. Zhang, S. Tang, Z. Li, S. Shen, C.-Y. Chiu, and R. Murch, "A novel reconfigurable intelligent surface for wide-angle passive beam-forming," *IEEE Trans. Microwave Theory Tech.*, vol. 70, no. 12, pp. 5427–5439, 2022.
- [12] J. Rao, Y. Zhang, S. Tang, Z. Li, C.-Y. Chiu, and R. Murch, "An active reconfigurable intelligent surface utilizing phase-reconfigurable reflection amplifiers," *IEEE Trans. Microwave Theory Tech.*, vol. 71, no. 7, pp. 3189–3202, 2023.
- [13] Y. Zhang, S. Shen, Z. Han, C.-Y. Chiu, and R. Murch, "Compact MIMO systems utilizing a pixelated surface: Capacity maximization," *IEEE Trans. Veh. Technol.*, vol. 70, no. 9, pp. 8453–8467, 2021.
- [14] Y. Zhang, Z. Han, S. Shen, C.-Y. Chiu, and R. Murch, "Polarization enhancement of microstrip antennas by asymmetric and symmetric grid defected ground structures," *IEEE Open J. Antennas Propag.*, vol. 1, pp. 215–223, 2020.

- [15] S. Shen, K.-K. Wong, and R. Murch, "Antenna coding empowered by pixel antennas," *IEEE Trans. Commun.*, vol. 74, pp. 446–460, 2026.
- [16] Z. Han, S. Shen, and R. Murch, "Exploiting spatial multiplexing based on pixel antennas: An antenna coding approach," *arXiv preprint arXiv:2512.05706*, 2025.
- [17] K.-K. Wong, A. Shojaeifard, K.-F. Tong, and Y. Zhang, "Fluid antenna systems," *IEEE Trans. Wirel. Commun.*, vol. 20, no. 3, pp. 1950–1962, 2021.
- [18] H. Yang, H. Xu, K.-K. Wong, C.-B. Chae, R. Murch, S. Jin, and Y. Zhang, "Position index modulation for fluid antenna system," *IEEE Trans. Wirel. Commun.*, vol. 23, no. 11, pp. 16 773–16 787, 2024.
- [19] Y. Huang, L. Xing, C. Song, S. Wang, and F. Elhouni, "Liquid antennas: Past, present and future," *IEEE Open J. Antennas Propag.*, vol. 2, pp. 473–487, 2021.
- [20] J. Zhang, J. Rao, Z. Li, Z. Ming, C.-Y. Chiu, K.-K. Wong, K.-F. Tong, and R. Murch, "A novel pixel-based reconfigurable antenna applied in fluid antenna systems with high switching speed," *IEEE Open J. Antennas Propag.*, vol. 6, no. 1, pp. 212–228, 2025.
- [21] W. K. New, K.-K. Wong, H. Xu, K.-F. Tong, and C.-B. Chae, "Fluid antenna system: New insights on outage probability and diversity gain," *IEEE Trans. Wirel. Commun.*, vol. 23, no. 1, pp. 128–140, 2024.
- [22] ———, "An information-theoretic characterization of MIMO-FAS: Optimization, diversity-multiplexing tradeoff and  $q$ -outage capacity," *IEEE Trans. Wirel. Commun.*, vol. 23, no. 6, pp. 5541–5556, 2024.
- [23] W. Ma, L. Zhu, and R. Zhang, "MIMO capacity characterization for movable antenna systems," *IEEE Trans. Wirel. Commun.*, vol. 23, no. 4, pp. 3392–3407, 2024.
- [24] Y. Ye, L. You, J. Wang, H. Xu, K.-K. Wong, and X. Gao, "Fluid antenna-assisted MIMO transmission exploiting statistical CSI," *IEEE Commun. Lett.*, vol. 28, no. 1, pp. 223–227, 2024.
- [25] J. Zou, H. Xu, C. Wang, L. Xu, S. Sun, K. Meng, C. Masouros, and K.-K. Wong, "Shifting the ISAC trade-off with fluid antenna systems," *IEEE Wirel. Commun. Lett.*, vol. 13, no. 12, pp. 3479–3483, 2024.
- [26] L. Zhou, J. Yao, M. Jin, T. Wu, and K.-K. Wong, "Fluid antenna-assisted ISAC systems," *IEEE Wirel. Commun. Lett.*, vol. 13, no. 12, pp. 3533–3537, 2024.
- [27] H. Gazzah and S. Marcos, "Cramer-Rao bounds for antenna array design," *IEEE Trans. Signal Process.*, vol. 54, no. 1, pp. 336–345, 2006.
- [28] CST Microwave Studio 2019, <http://www.cst.com>.
- [29] S. Shen, Y. Sun, S. Song, D. P. Palomar, and R. D. Murch, "Successive boolean optimization of planar pixel antennas," *IEEE Trans. Antennas Propag.*, vol. 65, no. 2, pp. 920–925, 2017.
- [30] F. Jiang, S. Shen, C.-Y. Chiu, Z. Zhang, Y. Zhang, Q. S. Cheng, and R. Murch, "Pixel antenna optimization based on perturbation sensitivity analysis," *IEEE Trans. Antennas Propag.*, vol. 70, no. 1, pp. 472–486, 2022.
- [31] T. Qiao, F. Jiang, S. Shen, Z. Zhang, M. Li, C.-Y. Chiu, Q. S. Cheng, and R. Murch, "Pixel antenna optimization using the adjoint method and the method of moving asymptote," *IEEE Trans. Antennas Propag.*, vol. 71, no. 3, pp. 2873–2878, 2023.
- [32] J. C. Bezdek and R. J. Hathaway, "Convergence of alternating optimization," *Neural, Parallel Sci. Comput.*, vol. 11, no. 4, pp. 351–368, 2003.